(Received 11 May 2025, Accepted 17 June 2025, Scheduled 29 June 2025)

Analysis of a Novel Hybrid-Excitation External-Rotor Switched Reluctance Motor

Liyun Feng[1, 2, 3] and Kaikai Diao[3, 4, *]

[1] School of Advanced Manufacturing Engineering, Hefei University, Hefei 230601, China
[2] Anhui Provincial Engineering Technology Research Center of Intelligent Vehicle Control and Integrated Design Technology Hefei 230601, China
[3] National Engineering Laboratory of Energy-Saving Motor and Control Technology, Anhui University, Hefei 230601, China
[4] School of Electrical Engineering and Automation, Anhui University, Hefei 230601, China

ABSTRACT: In this paper, a novel hybrid-excitation external-rotor switched reluctance motor is presented to solve the problem of low output torque of traditional switched reluctance motors (SRMs). The hybrid-excitation SRM, serving as an effective alternative to electric excitation SRMs, achieves comparable torque output with reduced excitation currents and lower power consumption within a certain range. First, the structural configuration and operational principles of the proposed SRM are presented and investigated. Then, key electromagnetic properties based on three-dimensional finite element analysis are analyzed in detail, such as the distribution of magnetic density, torque, and flux linkage. Furthermore, the validation is subsequently conducted through simulation data and performance comparisons with conventional outer-rotor 6/4 SRMs, conclusively confirming the theoretical framework's practical feasibility. Finally, the direct torque control with variable flux linkage based on the HESRM is executed, and the good control performance is verified under different conditions.

1. INTRODUCTION

The switched reluctance motor (SRM) has emerged as a preferred traction solution for electric vehicles (EVs), offering distinctive advantages including inherent fault tolerance, cost-effective manufacturing, simple structure, and exceptional robustness, and sustained operational efficiency across wide speed ranges [1]. Nevertheless, SRMs present inherent challenges including notable torque ripple and comparatively low torque density. These limitations have driven extensive research into innovative motor configurations and advanced design optimization methodologies. Aside from control strategies and algorithms [2, 3], extensive investigations regarding structural design and parameter optimization have been conducted to further reduce power consumption and increase electromagnetic torque [4, 5].

Over the past decades, traditional SRM configurations have been successfully designed and implemented. Furthermore, a series of novel topological structures have emerged as derivatives of conventional designs, aimed at either enhancing SRM performance and reliability or addressing specialized operational conditions. Concretely, the novel SRM configurations can be classified into segmented stator/rotor SRMs, hybrid-excitation SRMs, double-stator/rotor SRMs, skewed-teeth SRMs, and axial-flux SRMs, or their hybrid combinations.

As for segmented SRMs, the implementation of segmented design in SRM stator-rotor configurations enables a significant reduction of magnetic flux path length, thereby decreasing core losses. Furthermore, the inherent electromagnetic isolation in segmented architectures enhances operational reliability and fault tolerance. Segmented SRMs can be categorized into three primary configurations: stator-segmented SRMs, rotor-segmented SRMs, and SRMs combining both segmented stator and rotor. For instance, a two-phase E-core segmented-stator SRM [6], a novel segmented-stator SRM equipped with the multi-tooth structure [7], and a segmented-rotor SRM with alternating wide and narrow teeth [8] were proposed to improve the performance.

In terms of the hybrid-excitation SRM, permanent magnets (PMs) are introduced to improve the torque and power density. As reported in [9], a 12/8 hybrid excitation SRM based on a C-shaped segmented-stator was presented, which placed the PMs between the stator pole tips. Meanwhile, the effective winding arrangement will be narrowed, causing worse heat dissipation performance. Besides, PMs can also be integrated within stator teeth. However, this topological structure fundamentally compromises the mechanical integrity of the SRM assembly [10]. In order to avoid the above two problems, PMs can be placed between adjacent stator modules [11].

Regarding double-stator/rotor SRM [12], the influence of radial forces can be mitigated, thus improving the power density. As reported in [13], a novel double-stator SRM with the multi-tooth structure was investigated to minimize the torque ripple. Recent studies on double-stator SRM have primarily focused on optimizing radial forces to minimize vibration and acoustic noise. The double-rotor SRM, which provides two independent mechanical output ports, was presented in [14], hence suitable for the dual electromechanical energy conversion in the trans-

* Corresponding author: Kaikai Diao (diaokaikai@ahu.edu.cn).

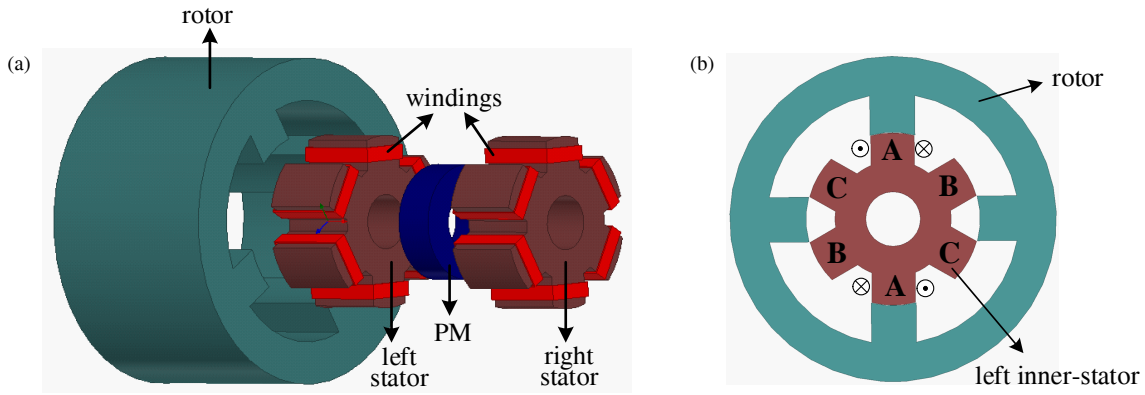

FIGURE 1. 3-D structure of HESRM. (a) Expanded view. (b) Front view.

mission system of hybrid electric vehicles. In addition, a segmented double-stator SRM was proposed to further reduce the volume [15].

The skewed-teeth SRMs can be roughly classified into three types, the stator-only, rotor-only, and stator-rotor combination skewing structures. To effectively reduce the vibration problem caused by radial force, scholars have conducted extensive research on skewed-teeth SRMs [16]. As reported in [17], the stator skewed-teeth alone is more effective than rotor skewed-teeth alone. Moreover, setting both the stator and rotor as the skewed-teeth structure is the most effective way to suppress vibration and torque ripple.

Due to the larger air gap surface, the axial-flux SRMs have a higher power density than radial SRMs [18], which is suitable for applications with relatively short axial lengths, such as hub motors. For instance, an axial-flux SRM with a C-shaped block stator and a rectangular block rotor was proposed to obtain higher power density, more flexible winding layout space, stronger heat dissipation effect, and fault-tolerance capability [19].

In this article, the idea of hybrid-excitation was introduced into the external-rotor type SRM. A hybrid-excitation external-rotor switched reluctance motor (HESRM) is proposed, which enhances output torque by incorporating an axially magnetized ring-shaped PM between the two inner stators.

The remainder of the article is structured as follows. In Section 2, the structure and operating principle of the HESRM are explained in detail. Section 3 illustrates the main characteristics including torque and flux linkage. Besides, the comparison results between the proposed structure and conventional SRM are provided. The direct torque control with variable flux linkage based on the HESRM is employed in Section 4, followed by the conclusion in Section 5.

2. TOPOLOGY AND PRINCIPLE

2.1. Topology of Proposed HESRM

Since the traditional SRM relies only on the electric excitation, the output torque performance is limited. Therefore, a PM is added in the inner-stator to increase torque at the same current. The three-dimensional (3-D) expanded view of the novel HESRM is shown in Fig. 1(a), which mainly consists of an outer-rotor, a hybrid inner-stator, and windings. It can be found that a hybrid inner-stator comprises a PM, a left inner-stator, and a right inner-stator. The proposed HESRM belongs to a three-phase SRM, and the poles of the outer-rotor and inner-stators are 4 and 6, respectively. The core materials of the inner and outer stators are DW310-35 silicon steel sheets, and the PM material is neodymium iron boron (NdFe30). Moreover, the PM is axially magnetized and radially configured in a ring shape, and its width is equal to the thickness of the stator yoke of the two inner-stator blocks. The tooth-pole structures and positional angles of the left and right inner-stator blocks are designed to be identical in both configuration and spatial orientation. Fig. 1(b) presents the front view of HESRM. As illustrated in Fig. 1(b), the two opposite tooth poles are connected in series as one phase, and the six tooth poles of the inner-stator are divided into phases A, B, and C. Phases B and C are respectively located at 60° and 120° in the clockwise direction of phase A.

2.2. Fundamental Equation

When inter-phase mutual inductance is neglected, the voltage equation of the motor is simplified to:

$$\begin{aligned} U_m &= R_m i + \frac{d\psi_m(\theta, i)}{dt} \\ &= R_m i + \frac{\partial \psi_m}{\partial \theta} \cdot \frac{d\theta}{dt} + \frac{\partial \psi_m}{\partial i} \cdot \frac{di}{dt} \end{aligned} \tag{1}$$

where θ and i are the rotor position angle and current; U_m, R_m, and ψ_m are phase voltage, resistance, and flux linkage of phase m, respectively.

The general torque considering the nonlinear region under saturation conditions can be expressed by the magnetic co-energy W_c as

$$T = \left.\frac{\partial W_c}{\partial \theta}\right|_{i_m=\text{const}}. \tag{2}$$

Furthermore, the instantaneous torque is expressed as

$$T \approx i\frac{\partial \psi_m(i, \theta)}{\partial \theta}. \tag{3}$$

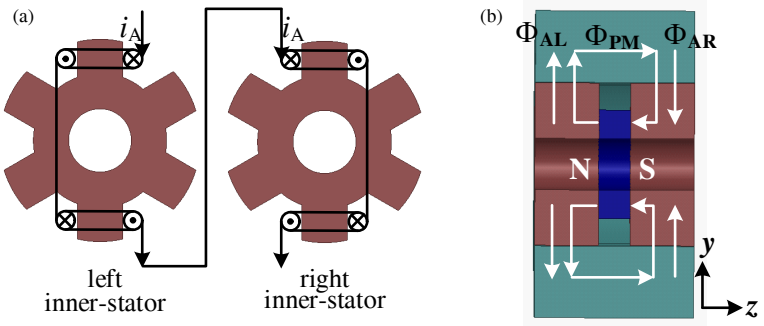

FIGURE 2. Winding and magnetic path. (a) Winding of the hybrid inner-stator. (b) Magnetic flux for producing torque.

The mechanical movement equation is defined as

$$T_e = T_L + D \cdot \omega + J\frac{d\omega}{dt} \tag{4}$$

where J, D, ω, T_L, and T_e are the moment of inertia, damping coefficient, mechanical angle velocity, load torque, and electromagnetic torque, respectively.

2.3. Principle of Proposed HESRM

Figure 2(a) shows the winding arrangement of phase A. It can be seen that the windings on the left and right inner-stators are connected in series. Obviously, the number of switching devices does not increase compared to the conventional 6/4 SRM. Fig. 2(b) shows the magnetic flux paths for producing torque including control and bias magnetic flux path. Φ_{PM} is the biased magnetic flux generated by the axially magnetized circular PM, and Φ_{AL} and Φ_{AR} are the control magnetic flux generated by the winding current from the hybrid inner-stator. The biased and control magnetic flux act together to generate the torque required by the system. The PM is axially magnetized to create a biased magnetic flux path, which forms a closed loop through the left inner-stator, rotor, and right inner-stator. The biased magnetic paths are respectively superimposed on the magnetic flux generated by the windings, which increases the electromagnetic torque.

3. ELECTROMAGNETIC CHARACTERISTICS

3.1. Distribution of Magnetic Density

The finite element model was established by using Ansys Maxwell software to simulate and analyze the electromagnetic characteristics of HESRM. As for the material setting, the BH curve of DW465_50 is shown in Fig. 3.

The rotor position angle θ is defined as 0° when the outer stator-teeth of phase A are unaligned with the rotor poles. Fig. 4 shows the 3-D distribution diagrams of the magnetic field distribution at 0° and 45° when phase A is energized, and the ampere-turns of the winding are set as 150 AT. It can be seen that the magnetic flux density of the motor is symmetrically distributed. The overall magnetic flux density at the alignment position is higher, and the magnetic pole density of the tooth-aligned portion is the largest. In the case of the above two different positions, the smallest part of the magnetic density appears in the yoke, and the magnetic density of the teeth is greater than that of the yoke totally. The magnetic density on the tooth poles of the HESRM is around 0.6 T to 1.3 T while that on the yoke is around 0.2 T to 0.5 T at 45°, and the maximum magnetic flux density is less than 1.2 T at 0°. Viewed axially, the magnetic density inside the HESRM is relatively higher than that at the external edge.

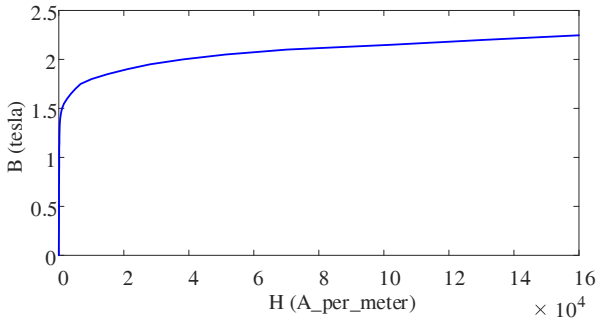

FIGURE 3. The BH curve of DW465_50.

Figure 5 shows the vector diagrams of magnetic field distribution in the absence or presence of current excitation at 45°. The ampere-turns of the winding are set as 150 AT when phase A is energized. As presented, the magnetic circuit passes through the left inner-stator, rotor, right inner-stator, and PM, and finally returns to the left inner-stator. The magnetic density with current excitation is totally greater than that without current excitation. The principle that the magnetic field generated by the winding is superimposed on the biased magnetic field generated by the PM to increase the torque is preliminarily verified. In addition, the conclusion is consistent with the magnetic flux density distribution, that is, the magnetic flux density of the teeth is greater than that of the yoke relatively.

3.2. Characteristics of Torque and Flux Linkage

More accurate static torque and the relationship curves of flux linkage with respect to angle and current can be obtained through Ansys/Maxwell finite element software. Fig. 6 shows static cogging torque characteristic when the rotor position angle ranges from 0° to 90°. As presented, the torque is relatively small, close to 0 Nm.

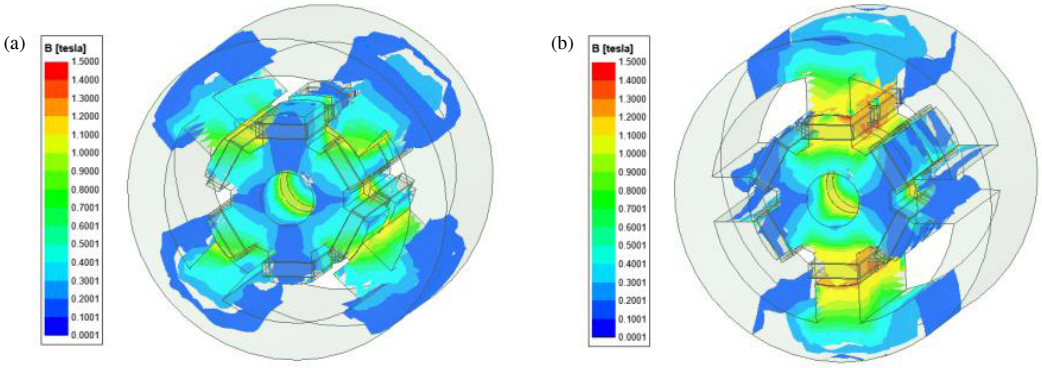

FIGURE 4. Magnetic flux density at (a) $\theta = 0°$, and (b) $\theta = 45°$.

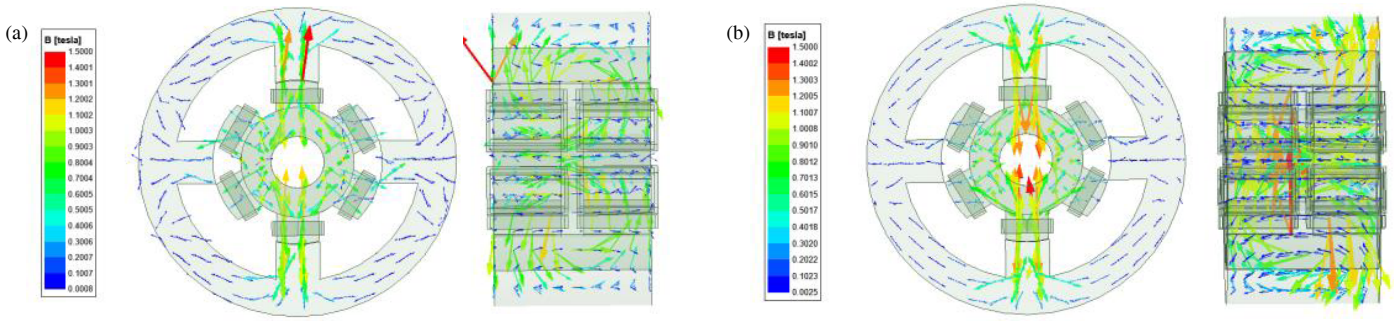

FIGURE 5. Vector diagram of magnetic flux density at 45°. (a) Without current excitation. (b) With current excitation.

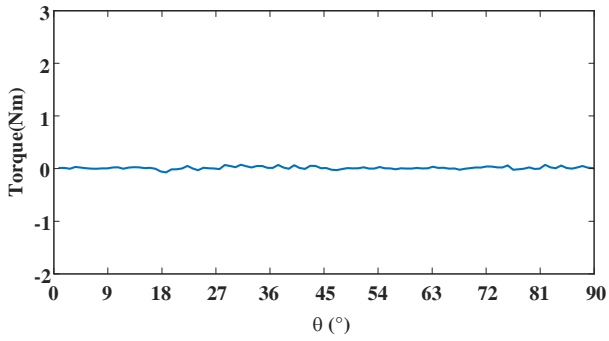

FIGURE 6. Cogging torque of the HESRM.

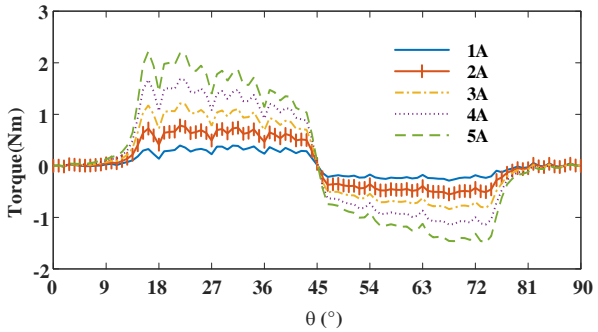

FIGURE 7. Torque characteristics of the HESRM.

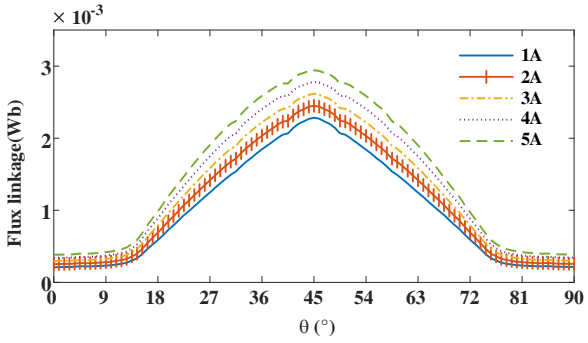

FIGURE 8. Flux linkage characteristics of the HESRM.

Figure 7 shows the static torque characteristic under different excitation current values of phase A when the rotor position angle ranges from 0° to 90°. As illustrated, the torque is zero when θ is at $-0°$, 45°, and 90° since the magnetic flux is symmetric, and there is no magnetic pull, which matches the principle of minimal reluctance. Obviously, the torque and current are positively correlated at the same rotor position angle. When θ is approximately 5°, the torque begins to rise sharply, which is related to the slope of the SRM magnetic co-energy variation curve. When the rotor rotates to about 16°, the torque with a value of approximately 2.2 Nm is the maximum under 5 A.

Figure 8 shows the static flux linkage characteristic under different excitation current values of phase A when the rotor position angle ranges from 0° to 90°. It can be obtained that the flux linkage nonlinearly increases as the HESRM operates within [0°, 45°] and decreases gradually within [45°, 90°]. The flux linkage reaches its maximum value when θ reaches the aligned position 0° under the same current. Similar to the torque, the flux linkage and current are also positively correlated at the same rotor position angle. Besides, the variation

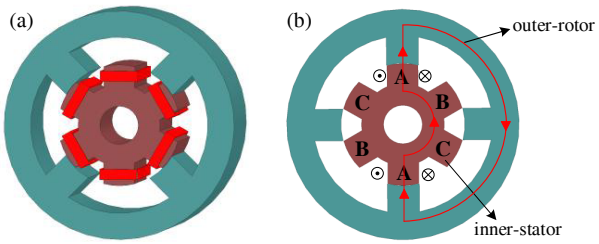

FIGURE 9. Structure of 6/4 outer-rotor SRM. (a) Expanded view. (b) Front view and winding excitation mode.

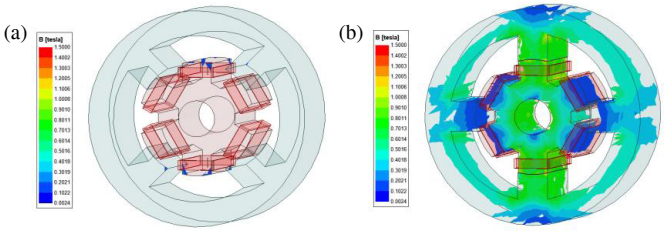

FIGURE 10. Magnetic flux density of conventional SRM. (a) $\theta = 0°$. (b) $\theta = 45°$.

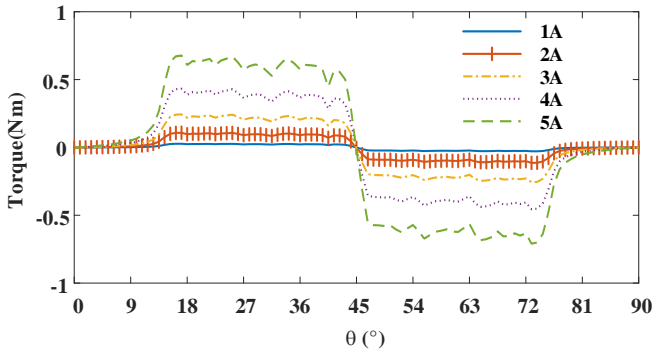

FIGURE 11. Torque characteristics of the conventional 6/4 outer-rotor SRM.

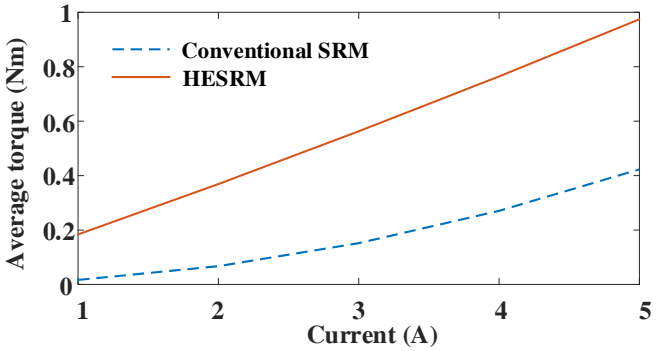

FIGURE 12. Comparison of average torque under different currents.

amplitude of the flux linkage is relatively small and gentle when the angles are within the ranges of [0°, 5°] and [85°, 90°].

3.3. Comparison of Characteristics

To verify the effectiveness of the proposed novel HESRM in enhancing torque output capability, a comparative analysis with a conventional 6/4 outer-rotor SRM was conducted. The expanded view of the conventional 6/4 outer-rotor SRM is presented in Fig. 9(a). Fig. 9(b) shows the front view and the winding excitation mode of phase A. As shown, in addition to the difference in the topology of the inner-stator, the winding excitation also differs from that of the HESRM. The magnetic circuit passes through the air gap from the inner stator to the outer rotor, then through the air gap, and finally returns to the inner stator to form a closed loop.

To ensure the fairness of the comparison, all dimensions except the PM are kept consistent, and the main dimension parameters of the two motors are listed in Table 1.

Figure 10 shows the magnetic field distribution at 0° and 45° when the ampere-turns of the winding are set as 150 AT. The magnetic density on the tooth poles of the HESRM is around 0.5 T to 0.9 T while that on the yoke is around 0.1 T to 0.5 T at 45°, and the maximum magnetic flux density is almost zero at 0°. Due to the absence of the PM, the magnetic flux density of conventional SRM is significantly lower than that of HESRM.

Figure 11 shows the torque characteristics of the conventional 6/4 outer-rotor SRM under the same current and size as the HESRM. It can be seen that the maximum value of the torque is approximately 0.7 Nm under 5 A when the rotor rotates to about 16°, which is 1.5 Nm lower than that of the HESRM. Obviously, the torque of the HESRM is higher than

TABLE 1. Main dimension parameters of two motors.

Parameters	Value
Rotor Outer Diameter/mm	67.5
Rotor Pole Arc	30
Rotor Inner Diameter/mm	36
Stator Outer Diameter/mm	35.7
Stator Inner Diameter/mm	11.3
Stator Pole Arc	32
Axial Length/mm	70
Air-gap Length/mm	0.3
PM Length/mm	10

that of conventional SRM. Furthermore, the torque waveform change is more gentle within [18°, 40°] and [50°, 75°] than that of HESRM.

For a more intuitive comparison, the comparison of HESRM and conventional SRM regarding average torque under different values of current is given in Fig. 12. Obviously, the value of average torque has been improved with the increase of the current. When the current varies from 1 to 5 A, the highest and lowest average torque values of HESRM are 0.18 Nm and 0.97 Nm while those of conventional SRM are 0.02 Nm and 0.42 Nm, respectively. It can be verified that the presented HESRM effectively improves the torque output capability of the system compared with the conventional SRM with electric excitation. Under the premise of generating the same magnitude of torque, the current required by the proposed HESRM is significantly smaller, which means that the torque-current ratio of HESRM is higher.

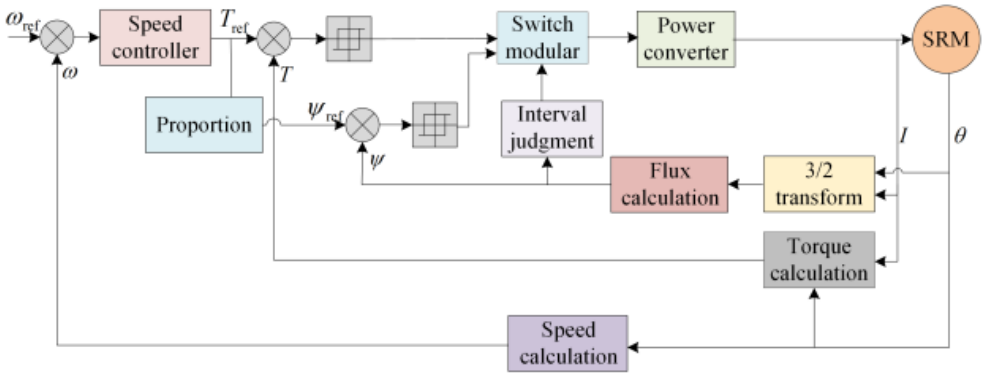

FIGURE 13. The block diagram of VF-DTC.

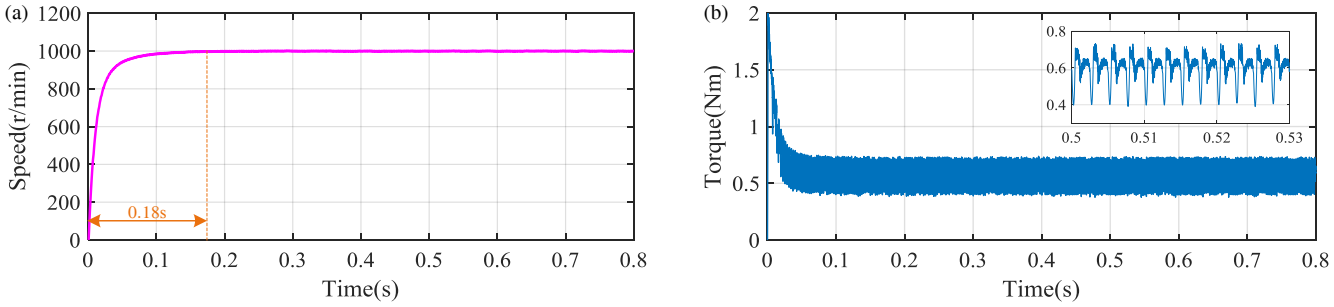

FIGURE 14. Simulation results under 0.6 Nm at 1000 r/min. (a) Speed. (b) Torque.

4. CONTROL SYSTEM BASED ON THE HESRM

4.1. DTC with Variable Flux Linkage

In this section, direct torque control with variable flux linkage (VF-DTC) is carried out based on the static torque and flux linkage data of the proposed HESRM to achieve good dynamic performance. Torque based on the phase relationship between flux linkages and variations in rotor position angle can be controlled. Compared with the DTC with a fixed given flux linkage, the flux linkage of the VF-DTC can be adaptively adjusted according to the demand for torque changes. The variable flux is applied to reduce the torque ripple and guarantee high-speed regulation, which behaves well in response time, robustness, anti-disturbance capability, and torque ripple reduction compared to the conventional DTC.

The block diagram of the control principle of the VF-DTC system is shown in Fig. 13. [20]. As shown, the outer-loop is a speed loop, and the difference between the reference speed and feedback speed is adjusted by the speed controller to output the reference torque. The inner-loop is composed of parallel torque loops and magnetic chain loops. The differences between the set values of each and the actual feedback values are limited within the hysteresis loop width to effectively suppress torque ripple. The appropriate voltage vector is selected based on the increase or decrease of torque and flux linkage, the judgment of flux linkage sectors, and the switch table, and then the conduction and turn-off of the switch are determined. The reference torque is approximately adjusted by the proportional coefficient as the control signal of the flux linkage. The relationship between the reference flux linkage and the reference torque T_{ref} is set as $\psi_{ref} = k_1 T_{ref} + k_2$, where k_1 and k_2 are adjustable coefficients.

4.2. Simulation Results

According to the control block diagram, a VF-DTC system based on HESRM can be built in Matlab/Simulink. The reference speed and load torque are set as 1000 r/min and 0.6 Nm, respectively. The simulation results regarding speed and torque in this condition are presented in Fig. 14. As illustrated, the initial response time of the speed is approximately 0.18 s, and then the speed achieves stable tracking. In terms of output torque, the maximum and minimum values of torque in the stable state are 0.4 Nm and 0.72 Nm, respectively. Therefore, the torque ripple is calculated as 53%. It can be seen that the VF-DTC based on HESRM behaves well in speed tracking and torque ripple reduction performance when the load torque and reference speed are set as 0.6 Nm and 1000 r/min, respectively.

The simulation results regarding speed and torque when the load torque is set as 0.6 Nm and a speed change (from 1000 to 1200 r/min) is applied at 0.4 s are presented in Fig. 15. As shown, the speed can still be stably tracked under the working condition of sudden changes in speed. The dynamic response time is about 0.13 s to return to the reference speed at 0.4 s. As for the torque performance, the maximum and minimum values of torque in the stable state are 0.37 Nm and 0.75 Nm under 1200 r/min, and the torque ripple is calculated as 63%. It can be seen that the torque ripple becomes larger as the reference speed increases. Furthermore, the average torque has ba-

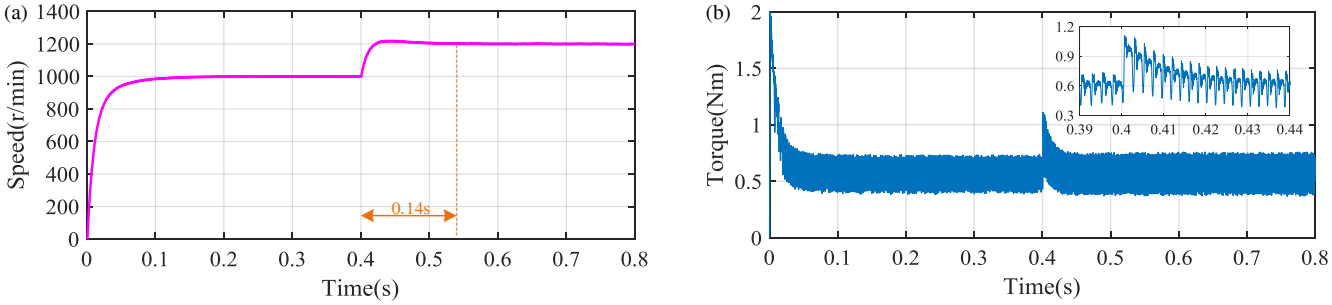

FIGURE 15. Simulation results under 0.6 Nm at speed change. (a) Speed. (b) Torque.

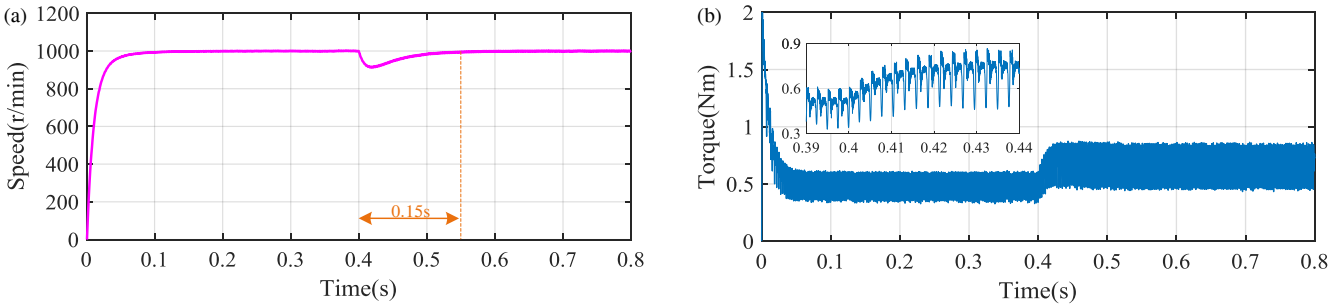

FIGURE 16. Simulation results under load torque change at 1000 r/min. (a) Speed. (b) Torque.

sically remained unchanged when the speed and torque ripples increase.

The simulation results regarding speed and torque when the reference speed is set as 1000 r/min and a load torque change (from 0.5 to 0.7 Nm) applied at 0.4 s are presented in Fig. 16. Obviously, the speed can still be stably tracked under the working condition of sudden changes in load torque. The dynamic response time to return to 1000 r/min and the speed overshoot are about 0.15 s and 86 r/min at 0.4 s, respectively. Regarding the torque, the maximum and minimum values of torque under 0.5 Nm are 0.35 Nm and 0.6 Nm, and the torque ripple is calculated as 50%. When the load torque changes to 0.7 Nm under 1000 r/min, the maximum and minimum values of torque are 0.45 Nm and 0.85 Nm, and the torque ripple is 57%. It can be known that both the average torque and torque ripple will change under load torque variation.

In conclusion, the VF-DTC based on HESRM can all achieve satisfactory control performance under various working conditions such as constant conditions, reference speed variations, and load torque variations based on the simulation results. For instance, the VF-DTC based on HESRM can provide good control performances including speed tracking, dynamic response, output torque, and anti-interference effect.

5. CONCLUSION

In this paper, a hybrid-excitation external-rotor switched reluctance motor (HESRM) has been presented. Compared with conventional SRM, the HESRM has the following advantages.

(1) The HESRM utilizes PM to provide axial biased magnetic flux, which improves the torque output capability and output power by using hybrid excitation instead of electric excitation.

(2) The HEBSRM has the superiority in lower required current and power consumption when generating the same average torque within a certain range according to the added PM.

(3) The control scheme of the conventional SRM is also applicable to the proposed novel structure, which will not increase the difficulty of the control scheme. As shown by the simulation results, the VF-DTC based on the proposed HESRM performed well in speed and output torque under different working conditions.

ACKNOWLEDGMENT

This work was supported by the Hefei University Talent Scientific Research Fund Project (24RC03) and in part by the National Engineering Laboratory of Energy-Saving Motor and Control Technology of Anhui University (KFKT202408).

REFERENCES

[1] Diao, K., X. Sun, G. Bramerdorfer, Y. Cai, G. Lei, and L. Chen, "Design optimization of switched reluctance machines for performance and reliability enhancements: A review," *Renewable and Sustainable Energy Reviews*, Vol. 168, 112785, 2022.

[2] Feng, L., X. Sun, G. Bramerdorfer, Z. Zhu, Y. Cai, K. Diao, and L. Chen, "A review on control techniques of switched reluctance motors for performance improvement," *Renewable and Sustainable Energy Reviews*, Vol. 199, 114454, 2024.

[3] Ding, S., X. Huang, J. Hang, and W. Li, "Improved efficiency optimization control of SRM based on redefined optimal turn-on angle and its corresponding analytical formula," *IEEE Transactions on Power Electronics*, Vol. 39, No. 12, 16 508–16 520, 2024.

[4] Yan, W., W. Wang, H. Li, H. Chen, F. Yu, D. Zhang, H. Yang, and Q. Wang, "Investigation on different stator structures of the axial-

radial flux switched reluctance motors," *IEEE Transactions on Industrial Electronics*, Vol. 71, No. 6, 5474–5484, 2024.

[5] Cai, J., B. Li, A. D. Cheok, Y. Yan, and X. Zhang, "Optimal design and control of a decoupled multi-frequency multi-phase wireless switched reluctance motor drive system," *IEEE Transactions on Power Electronics*, Vol. 39, No. 8, 10 152–10 165, 2024.

[6] Lee, C., R. Krishnan, and N. S. Lobo, "Novel two-phase switched reluctance machine using common-pole E-core structure: Concept, analysis, and experimental verification," *IEEE Transactions on Industry Applications*, Vol. 45, No. 2, 703–711, 2009.

[7] Mousavi-Aghdam, S. R., M. R. Feyzi, N. Bianchi, and M. Morandin, "Design and analysis of a novel high-torque stator-segmented SRM," *IEEE Transactions on Industrial Electronics*, Vol. 63, No. 3, 1458–1466, 2016.

[8] Mecrow, B. C., E. A. El-Kharashi, J. W. Finch, and A. G. Jack, "Segmental rotor switched reluctance motors with single-tooth windings," *IEE Proceedings — Electric Power Applications*, Vol. 150, No. 5, 591–599, 2003.

[9] Ding, W., S. Yang, Y. Hu, S. Li, T. Wang, and Z. Yin, "Design consideration and evaluation of a 12/8 high-torque modular-stator hybrid excitation switched reluctance machine for EV applications," *IEEE Transactions on Industrial Electronics*, Vol. 64, No. 12, 9221–9232, 2017.

[10] Masoumi, M. and M. Mirsalim, "E-core hybrid reluctance motor with permanent magnets inside stator common poles," *IEEE Transactions on Energy Conversion*, Vol. 33, No. 2, 826–833, 2018.

[11] Farahani, E. F., M. A. J. Kondelaji, and M. Mirsalim, "An innovative hybrid-excited multi-tooth switched reluctance motor for torque enhancement," *IEEE Transactions on Industrial Electronics*, Vol. 68, No. 2, 982–992, 2021.

[12] Abbasian, M., M. Moallem, and B. Fahimi, "Double-stator switched reluctance machines (DSSRM): Fundamentals and magnetic force analysis," *IEEE Transactions on Energy Conversion*, Vol. 25, No. 3, 589–597, 2010.

[13] Lee, C. H. T., K. T. Chau, C. Liu, T. W. Ching, and F. Li, "Mechanical offset for torque ripple reduction for magnetless double-stator doubly salient machine," *IEEE Transactions on Magnetics*, Vol. 50, No. 11, 1–4, 2014.

[14] Cui, S., Y. Yuan, and T. Wang, "Research on switched reluctance double-rotor motor used for hybrid electric vehicle," in *2008 International Conference on Electrical Machines and Systems*, 3393–3396, Wuhan, China, 2008.

[15] Guo, T., N. Schofield, and A. Emadi, "Double segmented rotor switched reluctance machine with shared stator back-iron for magnetic flux passage," *IEEE Transactions on Energy Conversion*, Vol. 31, No. 4, 1278–1286, 2016.

[16] Yang, H.-Y., Y.-C. Lim, and H.-C. Kim, "Acoustic noise/vibration reduction of a single-phase SRM using skewed stator and rotor," *IEEE Transactions on Industrial Electronics*, Vol. 60, No. 10, 4292–4300, 2013.

[17] Gan, C., J. Wu, M. Shen, S. Yang, Y. Hu, and W. Cao, "Investigation of skewing effects on the vibration reduction of three-phase switched reluctance motors," *IEEE Transactions on Magnetics*, Vol. 51, No. 9, 1–9, 2015.

[18] Torkaman, H., A. Ghaheri, and A. Keyhani, "Axial flux switched reluctance machines: A comprehensive review of design and topologies," *IET Electric Power Applications*, Vol. 13, No. 3, 310–321, 2019.

[19] Labak, A. and N. C. Kar, "Designing and prototyping a novel five-phase pancake-shaped axial-flux SRM for electric vehicle application through dynamic FEA incorporating flux-tube modeling," *IEEE Transactions on Industry Applications*, Vol. 49, No. 3, 1276–1288, 2013.

[20] Feng, L., X. Sun, X. Tian, and K. Diao, "Direct torque control with variable flux for an SRM based on hybrid optimization algorithm," *IEEE Transactions on Power Electronics*, Vol. 37, No. 6, 6688–6697, 2022.